Direct radiative effect of aerosols as determined from a combination of MODIS retrievals and GOCART simulations

Hongbin Yu,[1] R. E. Dickinson,[1] M. Chin,[2] Y. J. Kaufman,[2] M. Zhou,[1] L. Zhou,[1] Y. Tian,[1] O. Dubovik,[2] and B. N. Holben[2]

Received 25 June 2003; revised 1 December 2003; accepted 24 December 2003; published 12 February 2004.

[1] The aerosol direct solar effect under clear sky is assessed by (1) combining multiple aerosol characterizations and (2) using the satellite-retrieved land surface albedo. The aerosol characterization is made through an integration of the MODerate resolution Imaging Spectroradiometer (MODIS) retrievals and the Georgia Tech/Goddard Global Ozone Chemistry Aerosol Radiation and Transport (GOCART) model simulations. The spectral and bidirectional albedo of land surface is derived from MODIS. On a global average, the solar forcing at the top of atmosphere (TOA) DF_{TOA} is -4.5 Wm^{-2}, of which about 1/3 is contributed by a sum of natural and anthropogenic sulfate and carbonaceous aerosols. Though the optical depth is about 50% higher over land than over ocean, no significant land-ocean contrast in this TOA forcing is observed. It is reduced by larger aerosol absorption and higher surface albedo over land. As a result of absorption by soot and dust, a much larger surface cooling and substantial atmospheric absorption coexist over land and adjacent oceans. Globally, the surface cooling DF_{SFC} is about -9.9 Wm^{-2}, and the atmospheric absorption DF_{AIR} is about 5.4 Wm^{-2}, suggesting that more than half of the surface cooling results from the atmospheric absorption. Sensitivity tests show that an inclusion of MODIS-derived anisotropy of land surface reflection reduces the diurnal variation of TOA solar forcing, because of aerosol-induced changes in the fraction of direct beam and hence in the effective reflection from the surface. Constraining the GOCART dust absorption with recent measurements reduces DF_{AIR} and DF_{SFC} by 1.3 Wm^{-2} and 0.9 Wm^{-2}, respectively, and increases the TOA cooling by 0.4 Wm^{-2}. *INDEX TERMS:* 0305 Atmospheric Composition and Structure: Aerosols and particles (0345, 4801); 0360 Atmospheric Composition and Structure: Transmission and scattering of radiation; 0365 Atmospheric Composition and Structure: Troposphere—composition and chemistry; 1620 Global Change: Climate dynamics (3309); *KEYWORDS:* aerosols, radiative forcing, albedo

Citation: Yu, H., R. E. Dickinson, M. Chin, Y. J. Kaufman, M. Zhou, L. Zhou, Y. Tian, O. Dubovik, and B. N. Holben (2004), Direct radiative effect of aerosols as determined from a combination of MODIS retrievals and GOCART simulations, *J. Geophys. Res.*, *109*, D03206, doi:10.1029/2003JD003914.

1. Introduction

[2] Aerosols perturb the earth's energy budget directly by scattering and absorbing radiation [*Bohren and Huffman*, 1983; *Coakley et al.*, 1983] and indirectly by acting as cloud condensation nuclei and in doing so changing cloud properties [*Twomey*, 1977; *Albrecht*, 1989; *Rosenfeld*, 1999, 2000]. Their effects on temperature, hence atmospheric stratification, further influence clouds and so feedback on the radiation [*Hansen et al.*, 1997; *Ackerman et al.*, 2000]. The overall cooling by anthropogenic aerosols may be comparable to the warming of 2.43 Wm^{-2} by greenhouse gases [e.g., *Intergovernmental Panel on Climate Change* (*IPCC*), 2001; *Haywood and Boucher*, 2000]. However, large uncertainties exist in current estimates of aerosol forcing because of incomplete knowledge concerning the physical and chemical properties of aerosols as well as aerosol-cloud interactions. The uncertainty for the direct radiative forcing is about a factor of 2 to 3 and that for the indirect forcing is larger [*IPCC*, 2001]. These uncertainties complicate the assessment of aerosol impacts on surface-air interactions and the atmospheric boundary layer [*Yu et al.*, 2002; *Chung et al.*, 2002], global surface air temperatures and hydrology cycle [*Charlson et al.*, 1992; *Penner et al.*, 1992; *Kiehl and Briegleb*, 1993; *Hansen et al.*, 1997; *Ramanathan et al.*, 2001a; *Menon et al.*, 2002], photochemistry [*Dickerson et al.*, 1997; *Jacobson*, 1998], and ecosystems [*Chameides et al.*, 1999].

[3] Reduction of these uncertainties requires integrated research with multiple platforms (e.g., ground-based networks, satellite, ship, and aircraft) and techniques (e.g., in-situ measurement, remote sensing and computer modeling) [*Penner et al.*, 1994; *Heintzenberg et al.*, 1996; *Kaufman et al.*, 2002a; *Christopher and Zhang*, 2002]. We address this

[1]School of Earth and Atmospheric Sciences, Georgia Institute of Technology, Atlanta, Georgia, USA.
[2]NASA Goddard Space Flight Center, Greenbelt, Maryland, USA.

0148-0227/04/2003JD003914$09.00

issue by making use of improvements in aerosol modeling, satellite remote sensing, and Sun photometer measurement. Satellite remote sensing and computer modeling are needed to characterize the global spatial and temporal variations of aerosols. For this, we use data from the MODerate resolution Imaging Spectroradiometer (MODIS) onboard the Earth Observing System (EOS) satellites. This sensor is designed specifically for aerosol remote sensing and is acquiring separate aerosol optical depths (τ) for the fine mode and the coarse mode over ocean and vegetated land with near daily global coverage and high accuracy ($\pm 0.03 \pm 0.05\tau$ over ocean and $\pm 0.05 \pm 0.2\tau$ over land) [*Kaufman et al.*, 1997; *Tanre et al.*, 1997; *Chu et al.*, 2002; *Remer et al.*, 2002]. The Georgia Tech/Goddard Global Ozone Chemistry Aerosol Radiation and Transport (GOCART) model is used to simulate major atmospheric aerosol components using the assimilated meteorological fields [*Chin et al.*, 2000a, 2000b; *Ginoux et al.*, 2001; *Chin et al.*, 2002] and to interpret, complement, and extend both ground-based measurements and MODIS retrievals [e.g., *Chin et al.*, 2002; *Kaufman et al.*, 2002a; *Yu et al.*, 2003]. The data as obtained by combining MODIS and GOCART is evaluated with measurements from the AErosol RObotic NETwork (AERONET) which is an inclusive federation of ground-based aerosol network equipped well-calibrated Sun photometers from more than 100 field sites around the world [*Holben et al.*, 1998]. The AERONET provides relatively long-term record of aerosol optical depth, single-scattering albedo and asymmetry factor, among others [e.g., *Dubovik et al.*, 2000; *Dubovik and King*, 2000; *Holben et al.*, 2001; *Dubovik et al.*, 2002].

[4] The aerosol direct radiative forcing depends on the surface reflectance [e.g., *Coakley et al.*, 1983] that is anisotropic, wavelength dependent, and highly heterogeneous [e.g., *Dickinson*, 1983], making its characterization difficult and introducing additional uncertainty to the estimate of the aerosol direct effect. Aerosol radiative forcing calculations have usually used surface albedos that are determined or derived from land surface schemes in general circulation models [e.g., *Collins et al.*, 2002]. However, new satellite-borne instruments, such as MODIS and Multiangle Imaging Spectroradiometer (MISR), can much better characterize albedos because they measure the spectral variation and anisotropy of land surface reflection on a global scale at a high spatial resolution [*Schaaf et al.*, 2002; *Martonchik et al.*, 1998].

[5] This study calculates aerosol direct solar radiative forcing from optical depth obtained through a combination of MODIS retrievals and GOCART simulations [*Yu et al.*, 2003] and other aerosol optical properties (e.g., single-scattering albedo, Angstrom exponent, and asymmetry factor) taken from GOCART simulations. The MODIS land albedo products are used to characterize the heterogeneity and anisotropy of land surface reflection. These data sets and a radiative transfer model are described in Section 2. Section 3 presents seasonal variations and geographical patterns of aerosol direct solar effect, and discusses reasons for discrepancies between obtained in this study and other estimates. Sensitivity tests in Section 4 examine effects on the aerosol forcing by constraining the dust absorption with recent measurements and by including the anisotropy of surface reflection. Major conclusions are summarized in Section 5.

2. Description of Radiation Model and Data

2.1. Radiation Model

[6] Direct solar radiative perturbations by aerosols under a clear sky are calculated with a broadband, delta-four-stream radiative transfer model [*Fu and Liou*, 1992, 1993; *Fu et al.*, 1997]. The thermal infrared effect by aerosols is not addressed here. Computations with and without aerosols are compared to determine the monthly-averaged perturbations to solar radiation absorbed by the earth-atmosphere system (i.e., at the top of atmosphere, TOA), surface, and atmosphere, denoted as DF_{TOA}, DF_{SFC}, and DF_{AIR}, respectively. The surface forcing DF_{SFC} is the TOA forcing DF_{TOA} minus the atmospheric absorption DF_{AIR}. These use 30 minutes time steps over the month and varying the solar zenith angle appropriately. The *McClatchey et al.* [1972] climatology is used for temperature, water vapor and ozone. This simplification introduces an uncertainty of at most 5% in the aerosol solar perturbations [e.g., *Boucher and Tanre*, 2000] since dependences of aerosol extinction on humidity are included in MODIS retrievals and GOCART simulations.

[7] The model provides reasonable accuracy and compares well against a number of other radiative schemes in calculating aerosol TOA forcing [*Boucher et al.*, 1998; *Yu et al.*, 2002]. We show here the model performance on calculating the atmospheric absorption and surface cooling, as summarized by the ratio of the TOA forcing DF_{TOA} to the surface forcing DF_{SFC}, i.e., DF_{TOA}/DF_{SFC}. The ratio ranges from 1 for no atmospheric absorption to values less than 0 if aerosols contribute more to atmospheric warming than to surface cooling. Figure 1 shows its dependences on aerosol single-scattering albedo (ω_0), surface albedo (α), latitude, and aerosol optical depth (τ). Three broadband and SZA-independent values for α, namely 0.075, 0.15, and 0.3, are used, typical for ocean, vegetation, and desert, respectively. The diurnal average forcing ratio decreases strongly with increasing aerosol absorption and becomes smaller with larger surface albedo. Over dark oceanic surfaces (α of 0.075 or less) and a typical value of ω_0 over ocean of 0.95, this ratio is greater than 0.55. For a typical value of ω_0 over land of between 0.85 to 0.9, it reverses sign at α between 0.15 and 0.3. While the aerosol absorption is largest at the zenith, the aerosol upscattering is strongest at a solar zenith angle of about $60-70^\circ$ [e.g., *Boucher et al.*, 1998]. Hence, the forcing ratio is larger at high latitudes than at equator. An increase of aerosol optical depth increases the atmospheric absorption through multiple scattering and so reduces the ratio by a small amount.

[8] Our calculations are in good agreement with those of other studies using independent radiative transfer models. For example, at $\omega_0 = 0.95$, simulations with a Monte Carlo aerosol-cloud-radiation model [*Podgorny et al.*, 2000] give the diurnal average forcing ratio of 0.48 and 0.27 for a solar insolation condition of March 22 at 5°N over ocean and land, respectively [*Ramanathan et al.*, 2001a]. A similar simulation for $\omega_0 = 0.9$ derives a DF_{TOA}/DF_{SFC} of about 0.3 over ocean [*Podgorny and Ramanathan*, 2001]. *Collins et al.* [2002] use the NCAR CCM3 radiation scheme and derive

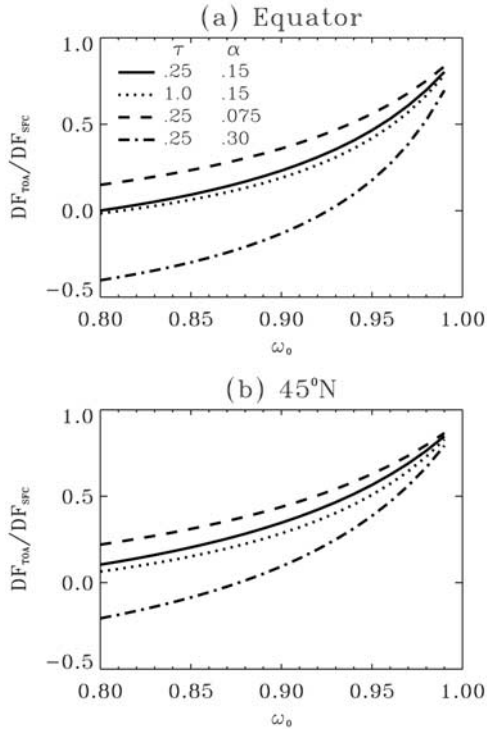

Figure 1. Changes of diurnal average DF_{TOA}/DF_{SFC} with aerosol single-scattering albedo (ω_0) for different values of optical depth (τ) and surface albedo (α). The calculations assume equinox insolation at (a) the Equator and (b) 45°N.

a DF_{TOA}/DF_{SFC} of about 0.3 for an average ω_0 of 0.877 over INDOEX region. A calculation with the MODerate resolution atmospheric TRANsmittance and radiation code version 4 (MODTRAN4) gives a DF_{TOA}/DF_{SFC} of 0.32 for $\omega_0 = 0.87$ in the Mediterranean [*Markowicz et al.*, 2002; *Lelieveld et al.*, 2002].

2.2. Aerosol Optical Properties

2.2.1. Optical Depth

[9] An annual cycle (November 2000–October 2001) of global aerosol optical depth at 550 nm has been obtained by integrating MODIS retrievals and GOCART model simulations with optimum interpolation [*Yu et al.*, 2003]. To facilitate later discussion, Figure 2 shows the spatial distributions of aerosol optical depth for April and October of 2001. In April, the aerosol optical depths in the northern hemisphere are among the highest of the year. Dust outbreaks and biomass burning elevate it to more than 0.4 over large parts of North Africa. In highly populated eastern China, it is as high as 0.6–0.8, from the combined effects of pollution, biomass burning in the south, and dust outbreaks in the north, while impacts extend to the North Pacific and even parts of North America [*Yu et al.*, 2003]. Optical depths are still high over North Africa in October, but are less in other regions in the northern hemisphere than in April. In contrast, over South Africa, South America, and tropical Atlantic Ocean, the optical depth is much higher in October than in April, from the biomass burning during the dry season.

[10] We estimate that the uncertainty of 20% for optical depth introduces a comparable uncertainty in the aerosol solar perturbations. Vertical profiles of aerosol extinction are less important than the columnar values for the estimate of the clear-sky solar radiative perturbations at TOA and surface [e.g., *Coakley et al.*, 1983], so a well mixed profile is assumed with a nominal mixing height of 2 km.

2.2.2. Single-Scattering Albedo

[11] Aerosol single-scattering albedo is the ratio of aerosol scattering to total extinction (a sum of scattering and absorption). If it is small, there is strong absorption by black carbon, mineral dust, and some organic carbons. A characterization of aerosol absorption or single-scattering albedo is complicated by instrument errors and modeling inadequacies, and these associated uncertainties/biases are major sources of uncertainty in studying aerosol-environmental interactions [e.g., *Heintzenberg et al.*, 1997]. The single-scattering albedo can not at present be retrieved by MODIS and so GOCART simulations are used to provide its spatial and temporal variations.

[12] These simulations provide concentrations of major aerosol components, including sulfate, organic carbon, black carbon, mineral dust, and sea-salt, and derive the radiative properties based on the prescribed size distribution, refractive index, and hygroscopic growth [*Chin et al.*, 2002, 2001]. As an example, Table 1 lists the values of single-scattering albedo at 550 nm for hydrophilic components at the relative humidity of 80% and for dust in a size

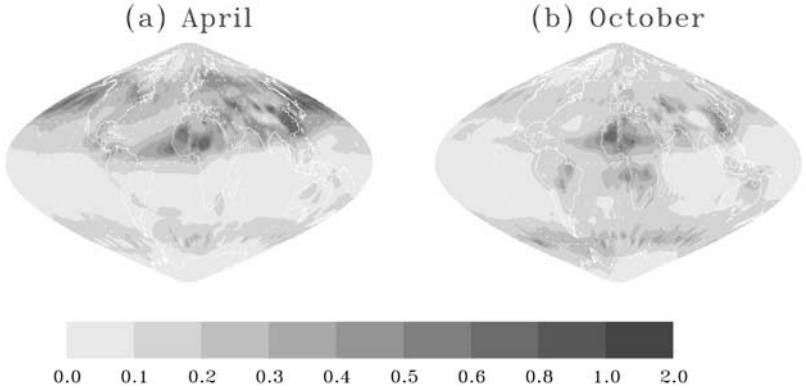

Figure 2. Aerosol optical depth at 550 nm from integration of MODIS retrievals and GOCART simulations for (a) April and (b) October [from *Yu et al.*, 2003]. See color version of this figure at back of this issue.

Table 1. Single-Scattering Albedos (ω_0) and Asymmetry Factor (g) at 550 nm for Sulfate (SU), Organic Carbon (OC), Black Carbon (BC), Sea Salt (SS) at the Relative Humidity of 80% and for Dust (DU) at Size Bin of 0.6–1.0 μm

	SU	OC	BC	SS	DU
ω_0	1.000	0.984	0.248	1.000	0.920
g	0.784	0.697	0.405	0.818	0.702

bin of 0.6–1.0 μm. An external mixing is assumed here in order to derive the single-scattering albedo for the mixture of all components. Comparisons show that about two thirds of differences between the derived absorptive optical depth (τ_{abs}) and AERONET climatology are within ±0.01, i.e., the uncertainty of AERONET measurements [*Dubovik et al.*, 2000; *Dubovik and King*, 2000; *Kaufman et al.*, 2002b]. Furthermore, when the AERONET data are separated with Angstrom exponent in the visible of less than 0.5, 0.5 to 1.5, and greater than 1.5 (corresponding to large, medium, and small particles), we find that the derived τ_{abs} at 550 nm is higher than the average over all AERONET observations by 0.014, −0.001, and −0.003, respectively. The overall bias of −0.0004 is much smaller than that found by *Sato et al.* [2003], because the assimilated optical depth is larger than the GOCART optical depth [*Yu et al.*, 2003].

[13] The high bias of τ_{abs} for large particles suggests that the absorptivity of dust is overestimated in the model, as confirmed by mounting evidence mainly from recent observations of Sahara dusts [e.g., *Clarke and Charlson*, 1985; *Kaufman et al.*, 2001; *Dubovik et al.*, 2002; *Cattrall et al.*, 2003]. We will use these observations as a constraint and assess its impacts on the radiative forcing in Section 4.1. The low bias of τ_{abs} for small particles suggests that the absorption by black carbon and organic carbon is underestimated, probably because of their low concentrations and/or the assumption of external mixture [*Sato et al.*, 2003; *Martins et al.*, 1998; *Jacobson*, 2000, 2001].

2.2.3. Angstrom Exponent and Asymmetry Factor

[14] The MODIS derives Angstrom exponents for the visible range over land and for both the visible and the near-infrared over ocean. These retrievals over land have large uncertainties, as affected by surface reflection, aerosol size and absorption [*Chu et al.*, 2002]. We characterize the spectral variation of aerosol optical depth by using Angstrom exponents derived from GOCART simulations at 450, 550, and 900 nm. These are extrapolated to wavelengths beyond 900 nm. Globally the GOCART Angstrom exponent (450 ∼ 900 nm) is about 24% lower than the AERONET Angstrom exponent (440 ∼ 870 nm). We also use the GOCART-derived asymmetry factor [*Chin et al.*, 2001, 2002]. Typical values for individual components are listed in Table 1. The GOCART inferred values are mostly larger by 0.02–0.04 than those inferred from the MODIS retrieval at 550 nm over ocean. Over land, they have on average a bias of about +0.05 in comparison to the AERONET climatology. The biases of Angstrom exponent and asymmetry factor suggest that the GOCART simulated aerosols may be too large in size, possibly as a result of their assumed size distributions or hygroscopic growth and removal mechanisms.

2.3. Surface Albedo

[15] MODIS retrieves the Bidirectional Reflectance Distribution Function (BRDF) parameters of global land surfaces at seven wavelengths [*Schaaf et al.*, 2002] and from these provides black-sky and white-sky albedos, for direct beam and diffuse beam respectively [*Schaaf et al.*, 2002]. The black-sky and white-sky albedo are obtained for various land cover classifications in snow-free regions for July 2001 using MODIS 0.25° × 0.25° land cover [*Friedl et al.*, 2002] and snow-cover [*Hall et al.*, 2002] mapping. Figure 3 shows the SZA-dependence of black-sky albedo for barren land, grassland, and evergreen needleleaf forest in July 2001. It increases with increasing solar zenith angle and equals the white-sky albedo at a SZA of about 55°. The near-infrared black-sky albedo varies more with SZA over vegetation than over barren land, but in the visible differences are generally small. To calculate global aerosol direct forcing, we use monthly white-sky land albedos from MODIS on Terra for the same period of aerosol data, including those at the two broadband intervals (0.4–0.7 μm and 0.7–5.0 μm). Gaps in MODIS land albedo are filled with simulations from a climate model [*Zhou et al.*, 2003]. A neglect of the angular dependence of the albedo introduces a small uncertainty of about 5% to the monthly average of TOA forcing, as discussed in Section 4.2.

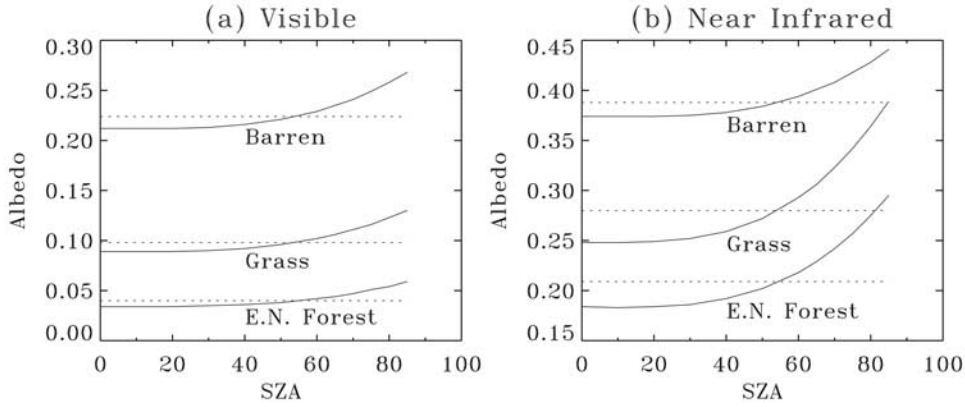

Figure 3. Dependence of land surface albedo in the visible (a) and in the near-infrared (b) on solar zenith angle (SZA) for barren land, grassland, and evergreen needleleaf forest, as inferred from MODIS BRDF retrievals. Solid and dotted lines denote black-sky albedo and white-sky albedo, respectively.

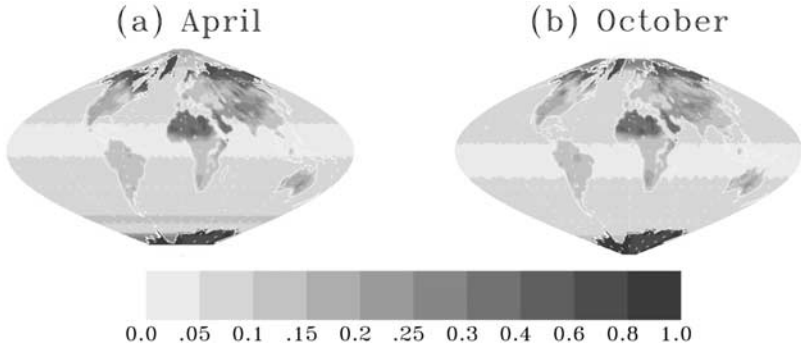

Figure 4. Composite of spectrally integrated monthly average MODIS land surface albedo [*Zhou et al.*, 2003] and ocean albedo [*Jin et al.*, 2002] for (a) April and (b) October. See color version of this figure at back of this issue.

[16] The spectral ocean albedo is derived from a look-up table that depends on solar zenith angle, wind speed, and chlorophyll concentration and is generated by a coupled atmosphere-ocean radiative transfer model [*Jin and Stamnes*, 1994; *Jin et al.*, 2002]. A constant wind speed of 10 ms^{-1}, no whitecaps [*Jin et al.*, 2002], and chlorophyll concentration of 1.0 mg m^{-3} are assumed in this study, resulting in an introduction of relatively small uncertainties (less than 10%) to the aerosol forcing calculations. A change of chlorophyll concentration from 0 to 10 mg m^{-3} changes the broadband ocean albedo by less than 0.005 [*Jin et al.*, 2002]. In the model, the wind-blown ocean surface roughness and ocean albedo increase with increasing wind speed, with a magnitude depending on the solar zenith angle (SZA) [*Jin et al.*, 2002]. An increase of wind speed from 2 ms^{-1} to 10 ms^{-1} increases the broadband ocean albedo by only 0.001 when SZA $\leq 60°$ but by as much as 0.06 when SZA = 80°. A wind speed of about 10 ms^{-1} generates whitecaps that increase the visible reflectance by 0.001 to 0.002 [*Moore et al.*, 2000].

[17] Figure 4 shows a composite of spectrally integrated surface albedo, as derived from ratios of the calculated monthly mean upwelling and downwelling fluxes at the surface. It is as high as 0.25–0.4 in the Saharan deserts and the Arabian Peninsula, and 0.2–0.3 in arid and semi-arid lands of west and central Asia. The surface at high latitudes also has an extremely high albedo, due to snow cover and sea ice. The ocean albedo in the tropics is lower than that at middle and high latitudes, resulting from its solar zenith angle dependence [*Jin et al.*, 2002]. The solar zenith dependence of ocean albedo gives a peak at about 60°S in April.

3. Results

[18] The aerosol solar perturbations are calculated using the data sets described in Section 2 for four representative months of January, April, July, and October in 2001. Similar patterns are observed in April and July, and in October and January, respectively. Discussion below focuses on the perturbations in April and October.

3.1. All Aerosols

[19] Figure 5 shows the solar perturbations DF_{TOA}, DF_{AIR}, and DF_{SFC} by all aerosols for April and October. Large geographical and seasonal variations are present. In the following, we discuss the aerosol direct effect in several distinct aerosol regions. Average values are listed in Table 2 for aerosol optical depth, single-scattering albedo, surface albedo, DF_{TOA}, and DF_{SFC} over regions as depicted in Figure 6.

[20] 1. North Africa and Arabian peninsula. The mineral dust dominates in the region and the solar perturbations are larger in April than in October, consistent with seasonal variations of dust storms. Dusts absorb solar radiation and enhance the atmospheric absorption by more than 15 Wm^{-2} in April. Over Saharan deserts and part of Arabian peninsula, the atmospheric absorption is more than the surface cooling, giving a positive DF_{TOA}. This results from interaction of modest dust absorptivity with high surface reflection. As a result, the Region D has the smallest TOA/surface forcing ratio, i.e., 0.06 in April and 0.13 in October. A similar warming effect also occurs at high latitudes of the northern hemisphere in April due to the presence of highly reflective snow. Continental dust over the tropical Atlantic also heats the atmosphere and cools the surface significantly, with a net cooling for the earth-atmosphere system (i.e., negative DF_{TOA}) because of a small ocean albedo.

[21] 2. South Asia. In April, the region is usually blanketed with thick brown haze with a single-scattering albedo of 0.87–0.90 [*Ramanathan et al.*, 2001b]. This gives rise to an atmospheric heating of more than 20 Wm^{-2} and the surface cooling of more than -30 Wm^{-2} over land. The average DF_{TOA} and DF_{SFC} over Region E is -4.4 and -16.4 Wm^{-2}, respectively, which is comparable to those from other studies over the northern Indian Ocean [e.g., *Ramanathan et al.*, 2001b; *Kaufman et al.*, 2002a; *Tahnk and Coakley*, 2002; *Collins et al.*, 2002] and Bay of Bengal [*Satheesh*, 2002]. In October, air in the region is cleaner and less absorbing, causing much smaller atmospheric heating and surface cooling.

[22] 3. East Asia and the northwestern Pacific. In April, the region has among the highest values in the world for atmospheric absorption and surface cooling. Aerosols increase atmospheric solar heating over the land by about 20 Wm^{-2}, resulting from large absorption by pollution in the region, and dusts from central Asia. The TOA/surface forcing ratio in Region F is about 1/3 on average. The outflow of the pollution and dust has far reaching impacts over the northwestern Pacific and even the northeastern Pacific, resulting in a TOA/surface forcing ratio of 0.48 in Region G. In October, air in the regions is less hazy and less

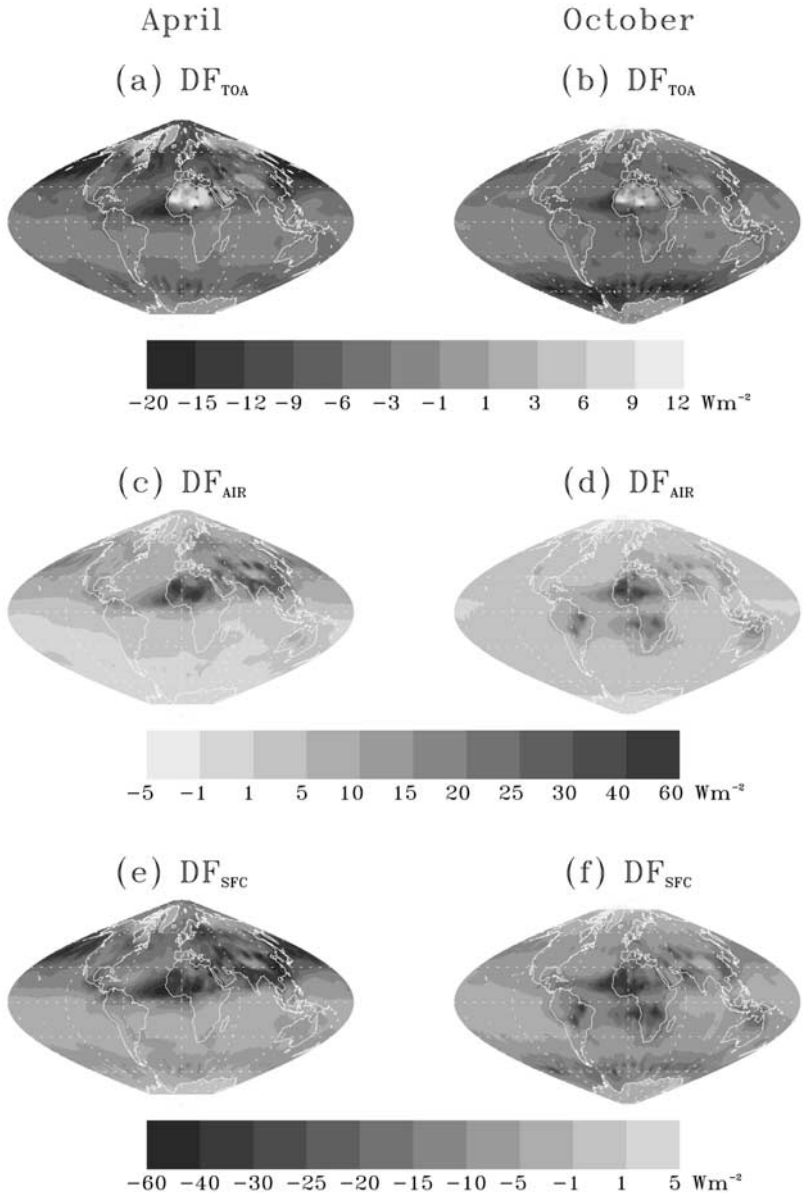

Figure 5. The direct solar perturbations (Wm^{-2}) at TOA (DF_{TOA}), atmosphere (DF_{AIR}) and surface (DF_{SFC}) by all aerosols for April (a, c, e) and October (b, d, f). See color version of this figure at back of this issue.

Table 2. Regional Averages of Optical Depth (τ), Single-Scattering Albedo (ω_0), Broadband Surface Albedo (α), TOA Forcing (DF_{TOA}, Wm^{-2}), and Surface Forcing (DF_{SFC}, Wm^{-2}) for April and October[a]

	April					October				
Region	τ	ω_0	α	DF_{TOA}	DF_{SFC}	τ	ω_0	α	DF_{TOA}	DF_{SFC}
A	0.24	0.92	0.12	−6.3	−16.1	0.14	0.93	0.12	−3.9	−7.7
B	0.23	0.94	0.06	−8.2	−15.6	0.15	0.94	0.07	−5.2	−8.7
C	0.30	0.92	0.11	−9.3	−21.4	0.18	0.92	0.12	−5.5	−10.7
D	0.36	0.90	0.23	−1.5	−24.2	0.32	0.90	0.23	−2.6	−19.5
E	0.19	0.87	0.06	−4.4	−16.4	0.15	0.93	0.06	−4.2	−8.8
F	0.44	0.92	0.14	−9.1	−28.0	0.25	0.93	0.13	−6.1	−13.4
G	0.45	0.93	0.07	−13.4	−28.1	0.17	0.95	0.07	−5.9	−9.6
H	0.08	0.94	0.08	−2.6	−5.2	0.18	0.89	0.08	−4.4	−14.2
I	0.11	0.99	0.10	−4.6	−5.3	0.17	0.97	0.08	−8.8	−11.4

[a]Symbols for regions are illustrated in Figure 6.

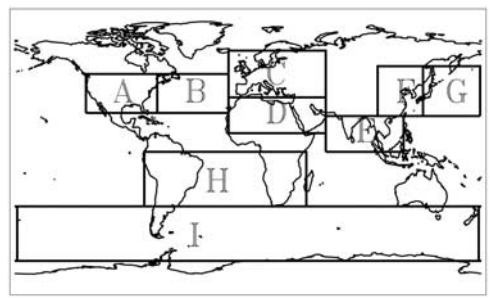

Figure 6. Illustration of regions selected for calculating average DF_{TOA} and DF_{SFC} in Table 2.

Table 3. Annual Averages of Optical Depth (τ), Clear-Sky Direct Solar Radiative Perturbations (DF, Wm^{-2}) by All Aerosols[a]

	MODIS + GOCART Integration					GOCART Alone				
	Global	N.H.	S.H.	Land	Ocean	Global	N.H.	S.H.	Land	Ocean
τ	0.142	0.186	0.098	0.183	0.128	0.120	0.157	0.083	0.164	0.106
DF_{TOA}	−4.5	−5.2	−3.8	−4.1	−4.6	−3.2	−3.8	−2.6	−4.1	−2.9
DF_{Air}	5.4	8.1	2.7	8.8	4.5	4.3	6.6	2.0	7.6	3.6
DF_{SFC}	−9.9	−13.3	−6.4	−12.9	−9.1	−7.5	−10.4	−4.6	−11.7	−6.5

[a]Two data sets of aerosol optical depth are used. Columns 2–6 represent calculations using the MODIS-GOCART assimilated optical depth, while columns 7–11 represent those using the GOCART optical depth only. Other aerosol parameters in both computations are taken from GOCART simulations.

absorbing and the magnitude of direct forcing reduces substantially.

[23] 4. North America and Europe. Pollution in these regions (Region A, B, and C) perturbs the solar radiation appreciably over the US-Atlantic-Europe corridor, more in April than in October. In April, the regions are cooled on average by 15 to 21 Wm^{-2} at the surface and 6 to 9 Wm^{-2} at the TOA, giving a TOA/surface forcing ratio of about 0.4 over land and 0.5 over ocean and smaller than the corresponding values of 0.5 and 0.6 in October.

[24] 5. South Africa and South America. The aerosol solar perturbations in April are small. In October, the biomass burning emits a large amount of soot particles to the atmosphere. The single-scattering albedo in October is the lowest anywhere in the world. It heats the atmosphere by as large as 15 to 25 Wm^{-2} and cools the surface by 15 to 30 Wm^{-2} over major biomass burning areas and over South Atlantic near the coast of South Africa. The average DF_{TOA} and DF_{SFC} over Region H is −4.4 and −14.2 Wm^{-2}, respectively, indicating that the atmospheric absorption by biomass burning smoke contributes to about 2/3 of the surface cooling.

[25] 6. Southern "roaring forties." This remote region (Region I) is dominated by nearly non-absorbing sea-salt aerosol and hence the TOA perturbation is close to the surface perturbation, having the largest TOA/surface forcing ratio of 0.8–0.9. The average surface cooling in October is about −11 Wm^{-2}, more than a factor of 2 larger than that in April. The surface albedo may be underestimated and hence the TOA radiative effect overestimated in this high-wind region from our assumption of constant wind speed of 10 ms^{-1}.

[26] Table 3 lists the four-month averages of aerosol optical depth and solar perturbations over the globe, northern hemisphere (N.H.), southern hemisphere (S.H.), land, and ocean. To illustrate how aerosol solar perturbations at individual latitude bands contribute to the global average, we show in Figure 7: zonal averages of DF_{TOA}, DF_{AIR}, and DF_{SFC} (Figure 7a), the ratio of DF_{TOA}/DF_{SFC} and the area-dependent weighting factor f for deriving the global average from zonal averages (Figure 7b), and the cumulative contribution (%) of zonal average forcing to the global average starting from the South Pole (Figure 7c). When using the MODIS-GOCART integration of optical depth, the respective global average forcing is −4.5, −9.9, and +5.4 Wm^{-2} for DF_{TOA}, DF_{SFC}, and DF_{AIR}, larger in April and July, and small in January and October (not shown). Differences as large as a factor of 2 for DF_{SFC} and 3 for DF_{AIR} exist between the northern hemisphere and the southern hemisphere, reflecting large impacts of anthropogenic activities in the northern hemisphere. Over land, the TOA cooling of −4.1 Wm^{-2} is less than but close to the −4.6 Wm^{-2} over ocean, due mainly to compensating effects of larger optical depth, smaller single-scattering albedo, and higher surface albedo over land. On the other hand, the surface is cooled and the atmosphere is heated more over land than over ocean. On a global average, the aerosol upscattering (i.e., TOA cooling) and the atmospheric absorption contribute nearly equally to the large surface cooling. As shown in Figure 7c, approximately 80–90% of DF_{SFC} and DF_{AIR} is contributed by aerosols in latitude bands of 30°S to 60°N, where the value of DF_{TOA}/DF_{SFC} is generally smaller than 0.5 (Figure 7b) because of large values of aerosol loading, absorption fraction, land mass and hence surface albedo. Contributions from other latitudes account for only 10–

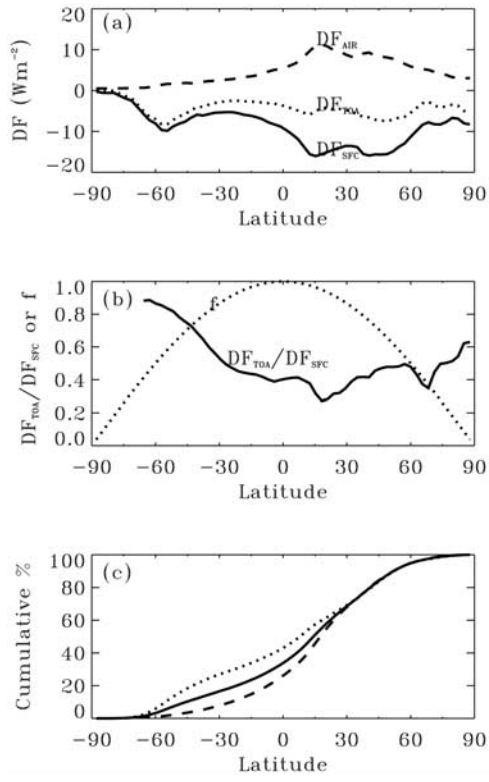

Figure 7. Latitudinal variations of (a) zonal averages of DF_{TOA}, DF_{AIR}, and DF_{SFC}, (b) the ratio of DF_{TOA}/DF_{SFC} (solid line) and the area-dependent weighting factor f (dotted line) for deriving the global average forcing from zonal averages, and (c) the cumulative contribution (%) of zonal average forcing to the global average starting from the South Pole (solid, dotted, and dashed lines denote DF_{SFC}, DF_{TOA}, and DF_{AIR}, respectively).

Table 4. Fractional Contributions of the MODIS Optical Depth to the Assimilated Optical Depth Used in Forcing Computations[a]

	Contribution
Global	0.64
N.H.	0.67
S.H.	0.56
Land	0.55
Ocean	0.67

[a]These fractions are weighted by the area of a grid box.

20%, because of relatively small aerosol forcing, weighting factor, absorption fraction, or combinations of them. As suggested by several recent studies, a combination of large atmospheric absorption and surface cooling can increase the stratification of lower atmosphere and has important implications for atmospheric circulations, global climate, hydrology cycle, and air pollution [e.g., *Ramanathan et al.*, 2001a; *Hansen et al.*, 1997; *Ackerman et al.*, 2000; *Yu et al.*, 2002].

[27] Also included in Table 3 is aerosol solar perturbations calculated with the GOCART optical depth. The GOCART optical depths are about 16% smaller than the assimilated optical depth, reducing the aerosol forcing by 20–30%. The differences are larger over ocean than over land, becuase of larger differences of optical depth over ocean, particularly over North Pacific and North Atlantic [*Yu et al.*, 2003]. We also look into relative contributions of MODIS retrievals and GOCART simulations to the aerosol loading (the assimilated optical depth) used in the forcing computations. Table 4 lists the fractional contribution of MODIS optical depth weighted by the area of a grid box. Clearly in the forcing calculations, MODIS represents 64% of the optical depth and GOCART the remaining 36%. MODIS contribution is lower (55%) over land than over ocean (67%), apparently because of lack of MODIS data over the deserts. MODIS contribution in the northern hemisphere is higher (67%) than in the southern hemisphere (56%) due to the higher optical depth from urban/industrial sources. These fractions should depend on the error parameters assumed for both MODIS and GOCART optical depths.

3.2. Anthropogenic Aerosols

[28] We calculate aerosol radiative perturbation by the sum of all sulfate, organic carbon, and black carbon and use it to estimate anthropogenic aerosol direct radiative forcing (ADF). On a global average, the so-derived anthropogenic aerosol optical depth is about 0.058, accounting for about 40% of the total optical depth. Anthropogenic aerosol is more absorbing and its absorption fraction is larger by 30–80% than that of all aerosols. Our identification of anthropogenic aerosol may introduce some biases. About 30% of sulfate comes from biogenic and volcanic sources and 10% of organic carbon from biogenic emissions and terpene oxidation [*IPCC*, 2001]. Some dusts are generated by human-induced land use change and some biomass burning can be ignited by lightning, but both are poorly quantified.

[29] The anthropogenic direct forcing ADF is calculated here by differentiating the radiative fluxes between with sulfate and carbonaceous aerosols only and without any aerosols. An alternative to the ADF calculation is to differentiate between total aerosols and natural aerosols (dust and sea-salt) only. Differences between the two scenarios, resulting from nonlinear dependence of forcing on optical depth and single-scattering albedo, are about 16% and 6%, for ADF_{TOA} and ADF_{SFC}, respectively. Table 5 lists the annual mean of anthropogenic aerosol optical depth and clear-sky anthropogenic direct radiative forcing. On global average, ADF_{TOA}, ADF_{AIR}, and ADF_{SFC} is estimated to be -1.4, $+2.8$, and -4.2 Wm^{-2}, respectively, accounting for 31%, 52%, and 42% of the corresponding perturbations by all aerosols (referring to Table 3). The values of ADF_{AIR} and ADF_{SFC} are nearly a factor of 2 larger over land and over the northern hemisphere than those over ocean and over the southern hemisphere. The relatively small difference of ADF_{TOA} that exists between land and ocean results from the combined effect of larger surface albedo and stronger aerosol absorption over land. The ratio of ADF_{TOA} to ADF_{SFC} is 1/3 on global average, smaller than the 0.46 for the total perturbation because anthropogenic aerosols are more absorbing than natural aerosols.

3.3. Comparisons With Other Studies

[30] Our estimated TOA forcing DF_{TOA} over ocean varies over the year from -4 to -5 Wm^{-2}, somewhat smaller than the estimate of -5 to -6 Wm^{-2} from the Polarization and Directionality of the Earth's Reflectances (POLDER) satellite retrievals without consideration of aerosol absorption [*Boucher and Tanre*, 2000] and -5.4 Wm^{-2} from the Sea-viewing Wide Field-of-view Sensor (SeaWiFS) [*Chou et al.*, 2002]. However, the corresponding atmospheric heating of 4.5 Wm^{-2} and the surface cooling of -9.9 Wm^{-2} are more than the 2.5 Wm^{-2} and -7.7 Wm^{-2} estimated from POLDER aerosol retrievals with a constraint by AERONET measurements in coastal regions [*Bellouin et al.*, 2003]. Our TOA/surface forcing ratio of 0.46 is smaller than their derived value of 0.67. As can be inferred from Figure 1, such a discrepancy may imply that their single-scattering albedo is greater than ours by about 0.03. This possible bias is comparable to the estimated accuracy for AERONET retrievals [e.g., *Dubovik et al.*, 2002]. In Section 4.1, we will assess how a constraint of dust absorption with recent measurements would reduce such biases. Past model-based estimates of clear-sky direct solar forcing over oceans range from -5.1 to -8.6 Wm^{-2} for DF_{TOA} and -7.4 to -10.8 Wm^{-2} for DF_{SFC}, with lower and upper ranges correspondig to a low and high sea-salt scenario respectively [*Haywood et al.*, 1999]. While our DF_{SFC} value falls in the middle of their range, the DF_{TOA} is close to the lower range of their estimates, suggesting a higher absorption in this study.

[31] *Takemura et al.* [2002], using aerosols and albedos simulated in a global model, give a DF_{TOA} that is a factor of 3 less than obtained here. Geographically, the most notable

Table 5. Annual Averages of Anthropogenic Aerosol Optical Depth (τ), Clear-Sky Anthropogenic Direct Radiative Forcing (ADF, Wm^{-2}) by Sulfate and Carbonaceous Aerosols

	Global	N.H.	S.H.	Land	Ocean
τ	0.058	0.087	0.029	0.085	0.049
ADF_{TOA}	−1.4	−1.9	−0.9	−1.8	−1.3
ADF_{AIR}	2.8	3.7	1.8	4.5	2.4
ADF_{SFC}	−4.2	−5.7	−2.7	−6.3	−3.6

Table 6. Comparison of Aerosol Optical Depth (τ) and Single-Scattering Albedo (ω_0) at 550 nm

	τ	ω_0
This study		
Land	0.183	0.923
Ocean	0.128	0.943
Takemura et al. [2002]		
Land	0.134	0.906
Ocean	0.093	0.945

differences exist over deserts and high latitudes. For example, the calculated TOA perturbation by *Takemura et al.* [2002] is a net absorption of more than 10 Wm^{-2} over the entire Saharan deserts and Arabian Peninsula in spring and summer (Figure 7 of *Takemura et al.* [2002]), due to the seemingly too strong solar absorption prescribed for mineral dusts. In this study, the TOA perturbation is smaller than +3 Wm^{-2} over half of these regions (Figure 5). We examine possible reasons for the discrepancy in the following.

[32] 1. Optical depth and single-scattering albedo. The discrepancy arises in part from different aerosol properties. We calculate average values of optical depth and single-scattering albedo (weighted by the optical depth) for land and ocean, respectively. As shown in Table 6, the optical depths of this study are 36% larger and the single-scattering albedo over land is 0.017 larger than corresponding values derived by *Takemura et al.* [2002]. DF_{TOA} estimated with these values and with typical values of albedo for land and ocean, is respectively about 85% larger over land and 35% larger over ocean than that by *Takemura et al.* [2002].

[33] 2. Time step. Aerosol direct solar perturbations change appreciably with the solar zenith angle [*Boucher et al.*, 1998] and hence different time steps for radiative calculations (30 minutes in this study and 3 hours in *Takemura et al.* [2002]) are expected to introduce some differences. Figure 8 shows the effect of time step on the calculated DF_{TOA}. The calculations are conducted at the longitude of 0°E and 30°E for equinox insolation. For a specific universal time (UT), the local solar time at the two longitudes differs by 2 hours and calculations sample the aerosol direct forcing for different solar zenith angles. For a time step of 30 min, the daily average DF_{TOA} is almost the same at longitude of 0°E and 30°E, as shown as solid line in Figure 8. For a time step of 3 hours, however, the calculated DF_{TOA} (dotted and dashed lines) biases either positively or negatively, depending on the longitude. Such biases are larger at low latitudes, because of rapid changes of solar zenith angle. When averaging along a latitude band or over the globe, the biases are largely canceled out. So the difference in the time step is not a major reason for the difference in the global average of aerosol solar perturbation.

[34] 3. Surface albedo. Potential differences in surface albedo between the two studies may also contribute to the discrepancy in aerosol forcing. Because no details of surface albedo are provided in *Takemura et al.* [2002], we cannot quantify such impacts. Our sensitivity tests do show that, for a respective increase of 0.05 and 0.1 in the surface albedo, DF_{TOA} decreases by about 10% and 20% for purely scattering aerosols. For strongly absorbing aerosols, the TOA perturbation is much sensitive to the surface albedo and may change from cooling to warming, although the respective surface perturbations change only by 7 and 14%.

4. Sensitivity Analysis

4.1. Constraining Dust Absorption With Measurements

[35] As discussed earlier, the aerosol direct effect has a stronger dependence on the single-scattering albedo over desert than over vegetation and ocean. The absorptive property of mineral dust, depending on the morphology and mineralogy, has been poorly quantified [*Sokolik et al.*, 2001]. There is emerging evidence [e.g., *Clarke and Charlson*, 1985; *Claquin et al.*, 1999; *Kaufman et al.*, 2001; *Haywood et al.*, 2001; *Dubovik et al.*, 2002; *Moulin et al.*, 2001; *Sinyuk et al.*, 2003; *Cattrall et al.*, 2003] that dust absorption could be much weaker than previously believed [e.g., *Patterson et al.*, 1977]. We assess how this new evidence will affect the estimates of aerosol direct forcing by using a combination of several measurements and retrievals of dust absorption.

[36] *Dubovik et al.* [2002] summarize that AERONET retrievals give the respective single-scattering albedo of 0.92, 0.95, 0.97, and 0.97 at 440, 670, 873, and 1022 nm for Saharan dusts. *Cattrall et al.* [2003] derive a respective value of 0.99 and 1.00 at 670 and 865 nm, significantly larger than that from AERONET measurments. Such a weaker absorption is also supported by *Kaufman et al.* [2001] and *Clarke and Charlson* [1985]. For pure dust, iron oxide (or rust) should reflect the solar radiation perfectly in the red and hence it is reasonable to use the single-scattering albedo of 1 in the red and beyond. As such, we use 0.92, 0.98, 1.0, and 1.0 to approximate the single-scattering albedo of pure dust at 440, 670, 873, and 1022 nm. Dusts with different origins may have different absorption, which is not considered here. These values are used to replace the GOCART prescribed single-scattering albedos for mineral dust and re-derive the single-scattering albedo for the aerosol mixture. Such a constraint reduces the dust absorption efficiency by about 50%, 40% and 100% at 450, 550, and 900 nm, respectively. Consequently, the atmospheric absorption DF_{AIR} is reduced by 1.3 Wm^{-2} (or 24%) globally, with a more reduction (-2.3 Wm^{-2}) over

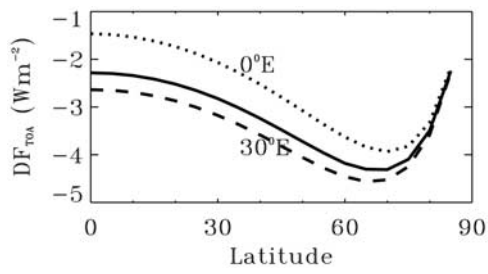

Figure 8. Sensitivity of aerosol TOA solar forcing (DF_{TOA}) to the time step of radiation calculation. The solid line is for a time step of 30 min and resembles calculations for two longitudes which can not be differentiated. Dotted and dashed lines are calculations with a time step of 3 hr at a longitude of 0°E and 30°E, respectively. Equinox insolation is assumed. Aerosol optical depth is 0.14 and single-scattering albedo is 0.94. Surface broadband albedo is 0.2.

land and less reduction (-1.0 Wm^{-2}) over ocean. Globally, the weaker dust absorption increases the TOA cooling by 0.4 Wm^{-2} (or 9%) and reduces the surface cooling by 0.9 Wm^{-2} (or 9%), increasing the DF_{TOA}/DF_{SFC} ratio from 0.46 (Table 3) to 0.54. Over land, the reduced DF_{AIR} is mainly balanced by the increased DF_{TOA} (-2.5 Wm^{-2}), with little change to the surface cooling. Over the Saharan deserts and Arabian peninsula, the TOA warming as shown in Figure 5 disappears. The largest TOA warming of about 10 Wm^{-2} changes to a TOA cooling of about -5 Wm^{-2}. Over ocean, the reduced DF_{AIR} is mainly balanced by a reduced surface cooling of 1.1 Wm^{-2}, with a little change to the TOA forcing. It appears that the constraint of dust absorption with measurements can explain about half of the differences of atmospheric absorption and surface cooling over ocean between this study and *Bellouin et al.* [2003] discussed in Section 3.3.

4.2. Effects of Anisotropy of Land Surface Reflection

[37] In principle, the determination of global albedo requires integrating the angular dependence of the albedo over a diurnal cycle of Sun angles with appropriate fractions of direct and diffuse solar beam, and its spectral dependence over different wavelengths, given the atmospheric attenuation by absorbing gases at each location. Aerosol extinction modifies the directional composition of incident solar radiation by increasing the diffuse beam and decreasing the direct beam. It also generates a spectral shift of solar fluxes due to the greater extinction at shorter wavelengths. These changes will alter the surface reflection and contribute to the aerosol TOA forcing additionally. The forcing changes due to the spectral shift have been considered through using visible and near-infrared albedos. Figure 9 shows that, when averaged over Sun angles, our approximation of using the white-sky albedo will introduce errors small compared to the errors already discussed.

[38] The dotted and dashed lines of Figure 9 represent simulations with the assumed fraction of direct beam (f_{dir}) of 0 and 1 respectively in calculating surface reflection. A realistic value of f_{dir} is in between 0 and 1 and the calculated aerosol forcing will fall between the green-dotted and black-dashed lines. Clearly, differences in DF_{TOA} resulting from using zenith angle dependence of albedos are relatively small, different from conclusions by *Coakley et al.* [1983]. They used a strong SZA-dependence for desert albedo, i.e., increasing from 0.07 at the zenith to 0.42 at the SZA of 60° (with an average of 0.3), and found that the angular dependence of surface reflection affects the TOA solar forcing significantly. For solid lines, an instantaneous albedo is calculated by combining the black-sky and white-sky albedo with the model generated f_{dir}. As such, forcing changes due to the aerosol-induced decrease of f_{dir} are accounted for. As can be inferred from Figure 3, a reduction of f_{dir} by aerosol increases the effective reflection at high Sun but decreases it at low Sun, larger over vegetation than over soil. Consequently, in comparison to those using a single albedo, the TOA forcing shifts towards a negative value (more cooling or less warming) at high Sun, but towards a positive value (less cooling) at low Sun.

[39] Although the differences seen in Figure 9 may be significant at a given Sun angle, they become much smaller with integration over solar zenith angles. The simplification of using the MODIS white-sky albedo in previous sections introduces a small uncertainty of 0.24 Wm^{-2} or 5% to the monthly average of TOA forcing over land. On the other hand, the anisotropy of surface reflection needs to be included when examining the diurnal variation of aerosol solar forcing. Further studies are needed to address this issue by using both MODIS and MISR albedo products.

5. Summary and Conclusions

[40] This study calculated aerosol direct radiative perturbations by combining MODIS retrievals and GOCART simulations of aerosols and by using MODIS retrievals of global land surface albedo. Although the optical depth is about 50% higher over land than over ocean, the land-ocean contrast in the TOA perturbation is reduced by a combination of larger aerosol absorption and higher surface reflection over land. On global and annual average, the estimated values for DF_{TOA}, DF_{AIR}, and DF_{SFC} are -4.5, $+5.4$, and -9.9 Wm^{-2}, respectively. About half of surface cooling results from the aerosol-induced atmospheric absorption. Geographically, a surface forcing that is more than a factor of 3 larger than the TOA forcing occurs over the Saharan deserts and Arabian penisula all year, South Asia and East Asia in April, South Africa and South America in Ocotber. The coexistence of substantial atmospheric absorption and surface cooling would induce a more stable lower atmosphere with important environmental implications.

[41] The calculated clear-sky TOA perturbation over ocean is quite close to the estimates from the POLDER [*Boucher and Tanre*, 2000] and the Sea-WiFS [*Chou et al.*, 2002] aerosol retrievals. But we have calculated more atmospheric absorption and surface cooling than estimated from POLDER [*Bellouin et al.*, 2003], likely a result of the smaller single-scattering albedo used in the model, for example, for mineral dusts. On global and annual average, the calculated clear-sky TOA perturbation is a factor of 3 larger than that estimated by *Takemura et al.* [2002], resulting from the use of relatively larger optical depths, weaker absorptions, and possibly different surface albedo in this study.

[42] The surface albedo affects aerosol-radiation interactions significantly. The MODIS provides an unprecedented opportunity for adequately characterizing the bidirectional and spectral reflectance of global land surface at a high resolution, reducing the uncertainty in the estimate of aerosol radiative forcing. Our sensitivity tests show that the inclusion of MODIS derived anisotropy of surface reflection reduces the diurnal variation of aerosol solar perturbations at the TOA, because aerosols reduce the fraction of direct beam and hence change the surface reflection. Such an effect is averaged out, if monthly or daily aerosol forcing is considered.

[43] Uncertainties associated with aerosol optical properties in general and single-scattering albedo in particular, introduce significant uncertainties to the calculation of radiative perturbations. Such uncertainties would be amplified over deserts and snow due to interactions of aerosol extinction with high surface reflection. Constraining the GOCART dust absorption with recent measurements reduces DF_{AIR} and DF_{SFC} by 1.3 Wm^{-2} and 0.9 Wm^{-2}, respectively. The TOA cooling is increased by 0.4 Wm^{-2}

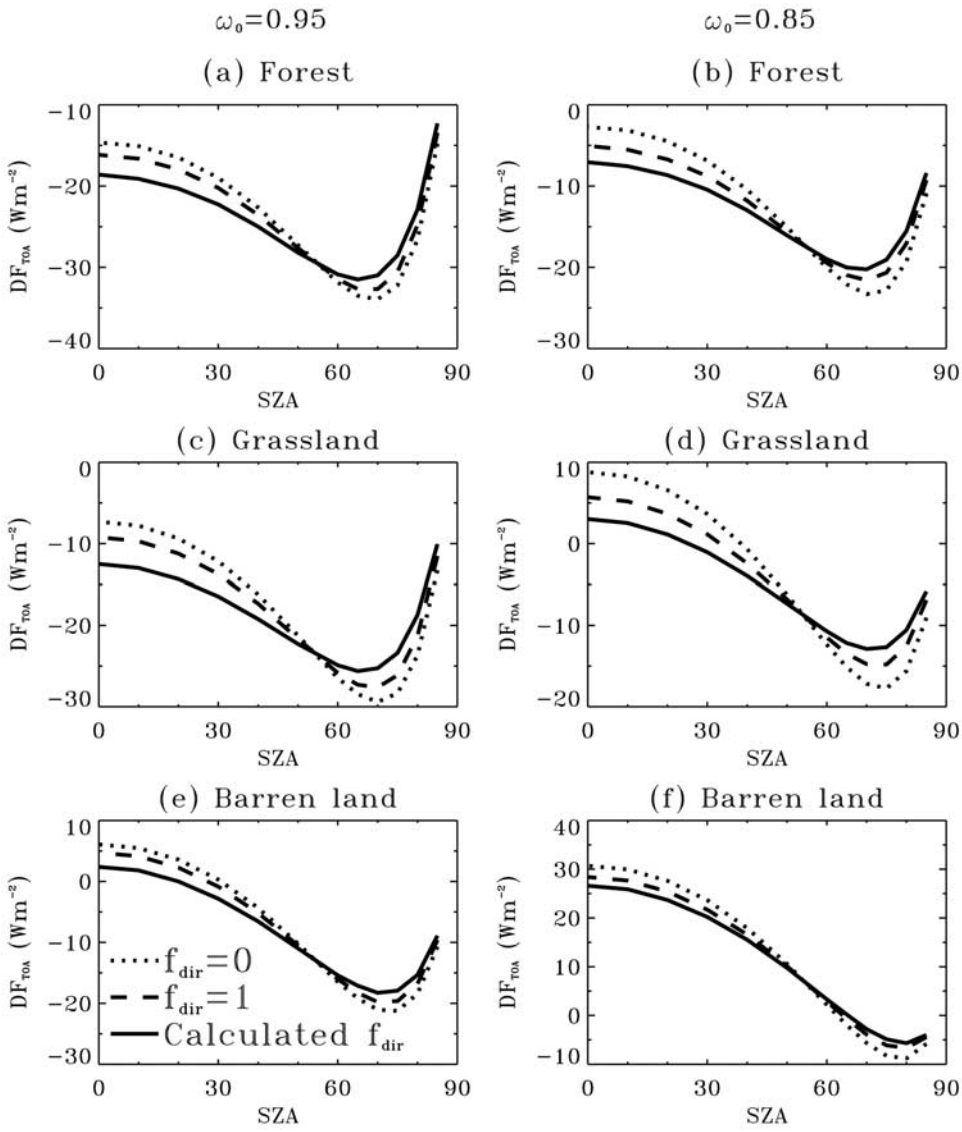

Figure 9. Diurnal variations of DF_{TOA} for three schemes of surface albedo and three types of land cover. Dotted and dashed lines represent calculations assuming the fraction of direct beam $f_{dir} = 0$ (i.e., the white-sky albedo) and $f_{dir} = 1$ (i.e., black-sky albedo), respectively. For solid lines, instantaneous values of surface albedo are calculated by combining black-sky and white-sky albedo with the model-generated f_{dir}. As such, the changes of aerosol forcing from the aerosol-induced changes of f_{dir} are included. Aerosol optical depth is 0.4 at 550 nm and the Angstrom exponent is 1. ω_0 denotes the aerosol single-scattering albedo and SZA stands for solar zenith angle.

(or 9%). The possible low bias of soot absorption needs to be addressed.

[44] In this study, we estimated that a sum of natural and anthropogenic sulfate and carbonaceous aerosols contributes about 1/3 to the total forcing of -4.5 Wm^{-2} at the TOA. A more accurate estimate of anthropogenic aerosol forcing needs an adequate separation of natural aerosols from anthropogenic aerosols. The thermal infrared radiative forcing was not calculated. For dusts, such a thermal infrared effect should be important but is highly uncertain [*Sokolik et al.*, 2001]. Its calculation requires vertical distributions of aerosol extinction and atmospheric temperature. Aerosol direct effect under cloudy-sky was also not considered. Calculations of the cloudy-sky aerosol direct effect require an adequate characterization of vertical distributions of aerosols and three-dimensional fields of clouds, especially for absorbing aerosols [*Liao and Seinfeld*, 1998]. Currently, substantial differences exist in aerosol vertical distributions simulated by different models and limited measurements do not suffice for their evaluation [*IPCC*, 2001]. The launch of spaceborne lidars in the near future should help improve the understanding of the thermal infrared forcing by dust and cloudy-sky aerosol radiative forcing.

[45] **Acknowledgments.** We appreciate the large efforts of MODIS and AERONET scientists in collecting and processing data used in this study. We are grateful to reviewers for their constructive suggestions that

have improved this manuscript significantly. Paul Ginoux is acknowledged for contributing to GOCART model simulations. We thank David Giles for updating the AERONET data for our analysis, Igor Podgorny and V. Ramanathan for providing helpful information about their Monte-Carlo modeling. The research was sponsored by the DOE SCIDAC project DE-FG02-01ER63198. H.Y. is grateful to the support from NASA GSFC AEROCENTER visiting scientist program. Mian Chin was supported by the NASA Radiation Science Program and Atmospheric Chemistry Modeling and Analysis Program (ACMAP).

References

Ackerman, A. S., O. B. Toon, D. E. Stevens, A. J. Heymsfield, V. Ramanathan, and E. J. Welton (2000), Reduction of tropical cloudiness by soot, *Science*, *288*, 1042–1047.

Albrecht, B. A. (1989), Aerosols, cloud microphysics, and fractional cloudiness, *Science*, *245*, 1227–1230.

Bellouin, N., O. Boucher, D. Tanre, and O. Dubovik (2003), Aerosol absorption over the clear-sky oceans deduced from POLDER-1 and AERONET observations, *Geophys. Res. Lett.*, *30*, 1748, doi:10.1029/2003GL017121.

Bohren, C. F., and D. R. Huffman (1983), *Absorption and Scattering of Light by Small Particles*, John Wiley, Hoboken, N. J.

Boucher, O., and D. Tanre (2000), Estimation of the aerosol perturbation to the Earth's radiative budget over oceans using POLDER satellite aerosol retrievals, *Geophys. Res. Lett.*, *27*, 1103–1106.

Boucher, O., et al. (1998), Intercomparison of models representing direct shortwave radiative forcing by sulfate aerosols, *J. Geophys. Res.*, *103*, 16,979–16,998.

Cattrall, C., K. L. Carder, and H. R. Gordon (2003), Columnar aerosol single-scattering albedo and phase function retrieved from sky radiance over the ocean: Measurements of Saharan dust, *J. Geophys. Res.*, *108*, 4287, doi:10.1029/2002JD002497.

Chameides, W. L., et al. (1999), A case study of the effects of atmospheric aerosols and regional haze on agriculture: An opportunity to enhance crop yields in China through emission controls?, *Proc. Natl. Acad. Sci.*, *96*(24), 13,626–13,633.

Charlson, R. J., S. E. Schwartz, J. H. Hales, R. D. Cess, J. A. Coakley Jr., J. E. Hansen, and D. J. Hofmann (1992), Climate forcing by anthropogenic aerosols, *Science*, *255*, 423–430.

Chin, M., R. B. Rood, S.-J. Lin, J.-F. Muller, and A. M. Thompson (2000a), Atmospheric sulfur cycle simulated in the global model GOCART: Model description and global properties, *J. Geophys. Res.*, *105*, 24,671–24,687.

Chin, M., D. L. Savoie, B. J. Huebert, A. R. Bandy, D. C. Thornton, T. S. Bates, P. K. Quinn, E. S. Saltzman, and W. J. De Bruyn (2000b), Atmospheric sulfur cycle simulated in the global model GOCART: Comparison with field observations and regional budgets, *J. Geophys. Res.*, *105*, 24,689–24,712.

Chin, M., P. Ginoux, B. Holben, M.-D. Chou, S. Kinne, and C. Weaver (2001), The GOCART model study of aerosol composition and radiative forcing, paper presented at 12th Symposium on Global Change and Climate Variations, Am. Meteorol. Soc., Albuquerque, N. M.

Chin, M., P. Ginoux, S. Kinne, O. Torres, B. Holben, B. N. Duncan, R. V. Martin, J. A. Logan, A. Higurashi, and T. Nakajima (2002), Tropospheric aerosol optical thickness from the GOCART model and comparisons with satellite and Sun photometer measurements, *J. Atmos. Sci.*, *59*, 461–483.

Chou, M.-D., P.-K. Chan, and M. Wang (2002), Aerosol radiative forcing derived from SeaWiFS-retrieved aerosol optical properties, *J. Atmos. Sci.*, *59*, 748–757.

Christopher, S. A., and J. Zhang (2002), Shortwave aerosol radiative forcing from MODIS and CERES observations over the oceans, *Geophys. Res. Lett.*, *29*, 1859, doi:10.1029/2002GL014803.

Chu, D. A., Y. J. Kaufman, C. Ichoku, L. A. Remer, D. Tanre, and B. N. Holben (2002), Validation of MODIS aerosol optical depth retrieval over land, *Geophys. Res. Lett.*, *29*, 8007, doi:10.1029/2001GL013205.

Chung, C. E., V. Ramanathan, and J. Y. Kiehl (2002), Effects of the South Asian absorbing haze on the northeastern monsoon and surface-air heat exchanges, *J. Clim.*, *15*, 2462–2476.

Claquin, T., M. Schulz, and Y. J. Balkanski (1999), Modeling the mineralogy of atmospheric dust sources, *J. Geophys. Res.*, *104*, 22,243–22,256.

Clarke, A. D., and R. J. Charlson (1985), Radiative properties of the background aerosol: Absorption component of extinction, *Science*, *229*, 263–265.

Coakley, J. A., Jr., R. D. Cess, and F. B. Yurevich (1983), The effect of tropospheric aerosols on the earth's radiation budget: A parameterization for climate models, *J. Atmos. Sci.*, *40*, 116–138.

Collins, W. D., P. J. Rasch, B. E. Eaton, D. W. Fillmore, J. T. Kiehl, C. T. Beck, and C. S. Zender (2002), Simulation of aerosol distributions and radiative forcing for INDOEX: Regional climate impacts, *J. Geophys. Res.*, *107*, 8028, doi:10.1029/2000JD000032.

Dickerson, R. R., et al. (1997), The impacts of aerosols on solar ultraviolet radiation and photochemical smog, *Science*, *278*, 827–830.

Dickinson, R. E. (1983), Land surface processes and climate-surface albedos and energy balance, *Adv. Geophys.*, *25*, 305–353.

Dubovik, O., and M. D. King (2000), A flexible inversion algorithm for retrieval of aerosol optical properties from Sun and sky radiance measurements, *J. Geophys. Res.*, *105*, 20,673–20,696.

Dubovik, O., A. Smirnov, B. N. Holben, M. D. King, Y. J. Kaufman, and I. Slutsker (2000), Accuracy assessments of aerosol optical properties retrieved from AERONET Sun and sky radiance measurements, *J. Geophys. Res.*, *105*, 9791–9806.

Dubovik, O., B. N. Holben, T. F. Eck, A. Smirnov, Y. J. Kaufman, M. D. King, D. Tanre, and I. Slutsker (2002), Variability of absorption and optical properties of key aerosol types observed in worldwide locations, *J. Atmos. Sci.*, *59*, 590–608.

Friedl, M. A., et al. (2002), Global land cover mapping from MOIDS: Algorithm and early results, *Remote Sens. Environ.*, *83*, 287–302.

Fu, Q., and K.-N. Liou (1992), On the correlated k-distribution method for radiative transfer in nonhomogeneous atmospheres, *J. Atmos. Sci.*, *49*, 2139–2156.

Fu, Q., and K.-N. Liou (1993), Parameterization of the radiative properties of cirrus clouds, *J. Atmos. Sci.*, *50*, 2008–2025.

Fu, Q., K.-N. Liou, M. C. Cribb, T. P. Charlock, and A. Grossman (1997), Multiple scattering parameterization in thermal infrared radiative transfer, *J. Atmos. Sci.*, *54*, 2799–2812.

Ginoux, P., M. Chin, I. Tegen, J. Prospero, B. Holben, O. Dubovik, and S.-J. Lin (2001), Sources and distributions of dust aerosols simulated with the GOCART model, *J. Geophys. Res.*, *106*, 20,225–20,273.

Hall, D. K., G. A. Riggs, V. V. Salomonson, N. E. DiGirolamo, and K. J. Bayr (2002), MODIS snow-cover products, *Remote Sens. Environ.*, *83*, 181–194.

Hansen, J., M. Sato, and R. Ruedy (1997), Radiative forcing and climate response, *J. Geophys. Res.*, *102*, 6831–6864.

Haywood, J., and O. Boucher (2000), Estimates of the direct and indirect radiative forcing due to tropospheric aerosols: A review, *Rev. Geophys.*, *38*, 513–543.

Haywood, J., V. Ramaswamy, and B. Soden (1999), Tropospheric aerosol climate forcing in clear-sky satellite observations over the oceans, *Science*, *283*, 1299–1303.

Haywood, J. M., P. N. Francis, M. D. Glew, and J. Taylor (2001), Optical properties and direct radiative effect of Saharan dust: A case study of two Saharan dust outbreaks using aircraft data, *J. Geophys. Res.*, *106*, 18,417–18,430.

Heintzenberg, J., H.-F. Graf, R. J. Charlson, and P. Warneck (1996), Climate forcing and the physico-chemical life cycle of the atmospheric aerosol - Why do we need an integrated, interdisciplinary global research programme?, *Contrib. Atmos. Phys.*, *69*, 261–271.

Heintzenberg, J., et al. (1997), Measurements and modeling of aerosol single-scattering albedo: Progress, problems and prospects, *Contrib. Atmos. Phys.*, *70*, 249–263.

Holben, B. N., et al. (1998), AERONET-A federated instrument network and data archive for aerosol characterization, *Remote Sens. Environ.*, *66*, 1–16.

Holben, B. N., et al. (2001), An emerging ground-based aerosol climatology: Aerosol optical depth from AERONET, *J. Geophys. Res.*, *106*, 12,067–12,098.

Intergovernmental Panel on Climate Change (IPCC) (2001), Radiative forcing of climate change, in *Climate Change 2001*, Cambridge Univ. Press, New York.

Jacobson, M. Z. (1998), Studying the effects of aerosols on vertical photolysis rate coefficient and temperature profiles over an urban airshed, *J. Geophys. Res.*, *103*, 10,593–10,604.

Jacobson, M. Z. (2000), A physically based treatment of elemental carbon optics: Implications for global direct forcing of aerosols, *Geophys. Res. Lett.*, *27*, 217–220.

Jacobson, M. Z. (2001), Strong radiative heating due to the mixing state of black carbon in atmospheric aerosols, *Nature*, *409*, 695–697.

Jin, Z., and K. Stamnes (1994), Radiative transfer in nonuniformly refracting layered media: Atmosphere-ocean system, *Appl. Opt.*, *33*, 431–442.

Jin, Z., T. P. Charlock, and K. Rutledge (2002), Analysis of broadband solar radiation and albedo over the ocean surface at COVE, *J. Atmos. Oceanic Technol.*, *19*, 1585–1601.

Kaufman, Y. J., D. Tanre, L. A. Remer, E. F. Vermote, A. Chu, and B. N. Holben (1997), Operational remote sensing of tropospheric aerosol over land from EOS moderate resolution imaging spectroradiometer, *J. Geophys. Res.*, *102*, 17,051–17,067.

Kaufman, Y. J., D. Tanre, O. Dubovik, A. Karnieli, and L. A. Remer (2001), Absorption of sunlight by dust as inferred from satellite and ground-based measurements, *Geophys. Res. Lett.*, *28*, 1479–1482.

Kaufman, Y. J., D. Tanre, and O. Boucher (2002a), A satellite view of aerosols in the climate system, *Nature*, *419*, doi:10.1038/nature01091.

Kaufman, Y. J., O. Dubovik, A. Smirnov, and B. N. Holben (2002b), Remote sensing of nonaerosol absorption in cloud free atmosphere, *Geophys. Res. Lett.*, *29*, 1857, doi:10.1029/2001GL014399.

Kiehl, J. T., and B. P. Briegleb (1993), The relative role of sulfate aerosols and greenhouse gases in climate forcing, *Science*, *260*, 311–314.

Lelieveld, J., et al. (2002), Global air pollution crossroads over the Mediterranean, *Science*, *298*, 794–799.

Liao, H., and J. H. Seinfeld (1998), Effects of clouds on direct aerosol radiative forcing of climate, *J. Geophys. Res.*, *103*, 3781–3788.

Markowicz, K. M., P. J. Flatau, R. V. Ramana, P. J. Crutzen, and V. Ramanathan (2002), Absorbing Mediterranean aerosols lead to a large reduction in the solar radiation at the surface, *Geophys. Res. Lett.*, *29*, 1968, doi:10.1029/2002GL015767.

Martins, J. V., P. Artaxo, C. Liousse, J. S. Reid, P. V. Hobbs, and Y. J. Kaufman (1998), Effects of black carbon content, particle size, and mixing on light absorption by aerosols from biomass burning in Brazil, *J. Geophys. Res.*, *103*, 32,041–32,050.

Martonchik, J. V., D. J. Diner, B. Pinty, M. M. Verstraete, R. B. Myneni, Y. Knjazikhin, and H. R. Gordon (1998), Determination of land and ocean reflective, radiative, and biophysical properties using multiangle imaging, *IEEE Trans. Geosci. Remote Sens.*, *36*, 1266–1281.

McClatchey, R. A., et al. (1972), Optical properties of the atmosphere, 3rd ed., *Rep. AFCRL-72-0497*, Air Force Cambridge Res. Lab., Hanscom Air Force Base, Mass.

Menon, S., J. Hansen, L. Nazarenko, and Y. Luo (2002), Climate effects of black carbon aerosols in China and India, *Science*, *297*, 2250–2253.

Moore, K., K. J. Voss, and H. R. Gordon (2000), Spectral reflectance of whitecaps: Their contribution to water-leaving radiance, *J. Geophys. Res.*, *105*, 6493–6499.

Moulin, C., H. R. Gordon, V. F. Banzon, and R. H. Evans (2001), Assessment of Saharan dust absorption in the visible from SeaWiFS imagery, *J. Geophys. Res.*, *106*, 18,239–18,249.

Patterson, E. M., D. A. Gillete, and B. H. Stockton (1977), Complex index of refraction between 300 and 700 nm for Saharan aerosol, *J. Geophys. Res.*, *82*, 3153–3160.

Penner, J. E., R. E. Dickinson, and C. A. O'Neill (1992), Effects of aerosol from biomass burning on the global radiation budget, *Science*, *256*, 1432–1434.

Penner, J. E., et al. (1994), Quantifying and minimizing uncertainty of climate forcing by anthropogenic aerosols, *Bull. Am. Meteorol. Soc.*, *75*, 375–400.

Podgorny, I. A., and V. Ramanathan (2001), A modeling study of the direct effect of aerosols over the tropical Indian Ocean, *J. Geophys. Res.*, *106*, 24,097–24,105.

Podgorny, I. A., W. C. Conant, V. Ramanathan, and S. K. Satheesh (2000), Aerosol modulation of atmospheric and solar heating over the tropical Indian Ocean, *Tellus, Ser. B*, *52*, 947–958.

Ramanathan, V., P. J. Crutzen, J. L. Kiehl, and D. Rosenfeld (2001a), Aerosols, climate, and the hydrological cycle, *Science*, *294*, 2119–2124.

Ramanathan, V., et al. (2001b), Indian Ocean Experiment: An integrated analysis of the climate forcing and effects of great Indo-Asian haze, *J. Geophys. Res.*, *106*, 28,371–28,398.

Remer, L. A., et al. (2002), Validation of MODIS aerosol retrieval over ocean, *Geophys. Res. Lett.*, *29*, 8008, doi:10.1029/2001GL013204.

Rosenfeld, D. (1999), TRMM observed first direct evidence of smoke from forest fires inhibiting rainfall, *Geophys. Res. Lett.*, *26*, 3105–3108.

Rosenfeld, D. (2000), Suppression of rain and snow by urban and industrial air pollution, *Science*, *287*, 1793–1796.

Satheesh, S. K. (2002), Radiative forcing by aerosols over Bay of Bengal region, *Geophys. Res. Lett.*, *29*, 2083, doi:10.1029/2002GL015334.

Sato, M., J. Hansen, D. Koch, A. Lacis, R. Ruedy, O. Dubovik, B. Holben, M. Chin, and T. Novakov (2003), Global atmospheric black carbon inferred from AERONET, *Proc. Natl. Acad. Sci.*, *100*, 6319–6324, doi:10.1073/pnas.0731897100.

Schaaf, C. B., et al. (2002), First operational BRDF, albedo and nadir reflectance products from MODIS, *Remote Sens. Environ.*, *83*, 135–148.

Sinyuk, A., O. Torres, and O. Dubovik (2003), Combined use of satellite and surface observations to infer the imaginary part of refractive index of Saharan dust, *Geophys. Res. Lett.*, *30*, 1081, doi:10.1029/2002GL016189.

Sokolik, I. N., et al. (2001), Introduction to special section: Outstanding problems in quantifying the radiative impacts of mineral dust, *J. Geophys. Res.*, *106*, 18,015–18,027.

Tahnk, W. R., and J. A. Coakley (2002), Aerosol optical depth and direct radiative forcing for INDOEX derived from AVHRR: Observations, January–March 1996–2000, *J. Geophys. Res.*, *107*, 8010, doi:10.1029/2000JD000183.

Takemura, T., T. Nakajima, O. Dubovik, B. Holben, and S. Kinne (2002), Single-scattering albedo and radiative forcing of various aerosol species with a global three-dimensional model, *J. Clim.*, *15*(4), 333–352.

Tanre, D., Y. J. Kaufman, M. Herman, and S. Mattoo (1997), Remote sensing of aerosol properties over oceans using the MODIS/EOS spectral radiances, *J. Geophys. Res.*, *102*, 16,971–16,988.

Twomey, S. (1977), The influence of pollution on the shortwave albedo of clouds, *J. Atmos. Sci.*, *34*, 1149–1152.

Yu, H., S. C. Liu, and R. E. Dickinson (2002), Radiative effects of aerosols on the evolution of the atmospheric boundary layer, *J. Geophys. Res.*, *107*, 4142, doi:10.1029/2001JD000754.

Yu, H., R. E. Dickinson, M. Chin, Y. J. Kaufman, B. N. Holben, I. V. Geogdzhayev, and M. I. Mishchenko (2003), Annual cycle of global distributions of aerosol optical depth from integration of MODIS retrievals and GOCART model simulations, *J. Geophys. Res.*, *108*, 4128, doi:10.1029/2002JD002717.

Zhou, L., et al. (2003), Comparisons of seasonal and spatial variations of albedos from MODIS and Common Land Model, *J. Geophys. Res.*, *108*, 4488, doi:10.1029/2002JD003326.

M. Chin and Y. J. Kaufman, Laboratory for Atmospheres, NASA Goddard Space Flight Center, Greenbelt, MD 20771, USA.

R. E. Dickinson, Y. Tian, H. Yu, L. Zhou, and M. Zhou, School of Earth and Atmospheric Sciences, Georgia Institute of Technology, Atlanta, GA 30332, USA. (yu@breeze.eas.gatech.edu)

O. Dubovik and B. N. Holben, Biospheric Sciences Branch, NASA Goddard Space Flight Center, Greenbelt, MD 20771, USA.

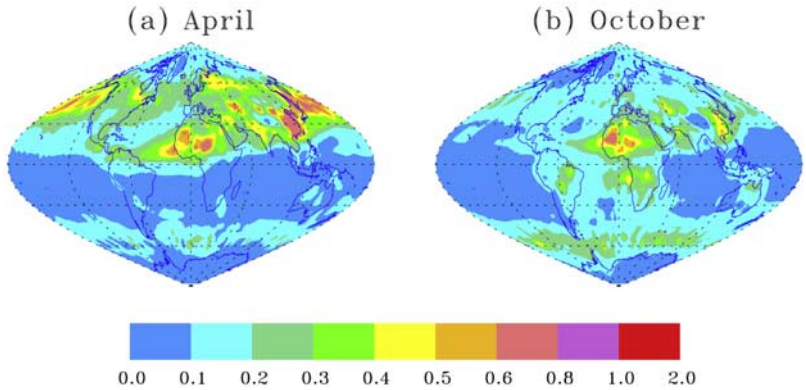

Figure 2. Aerosol optical depth at 550 nm from integration of MODIS retrievals and GOCART simulations for (a) April and (b) October [from *Yu et al.*, 2003].

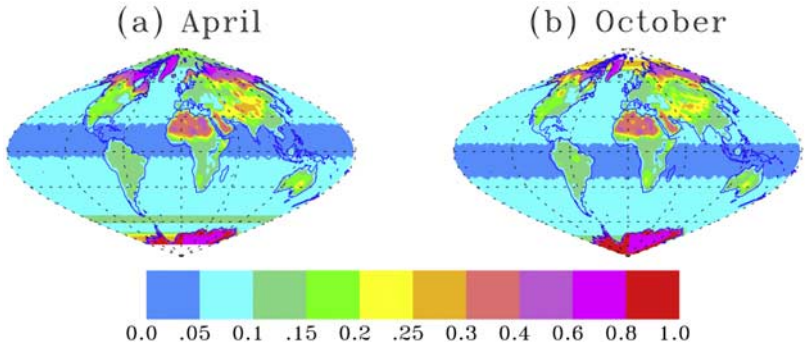

Figure 4. Composite of spectrally integrated monthly average MODIS land surface albedo [*Zhou et al.*, 2003] and ocean albedo [*Jin et al.*, 2002] for (a) April and (b) October.

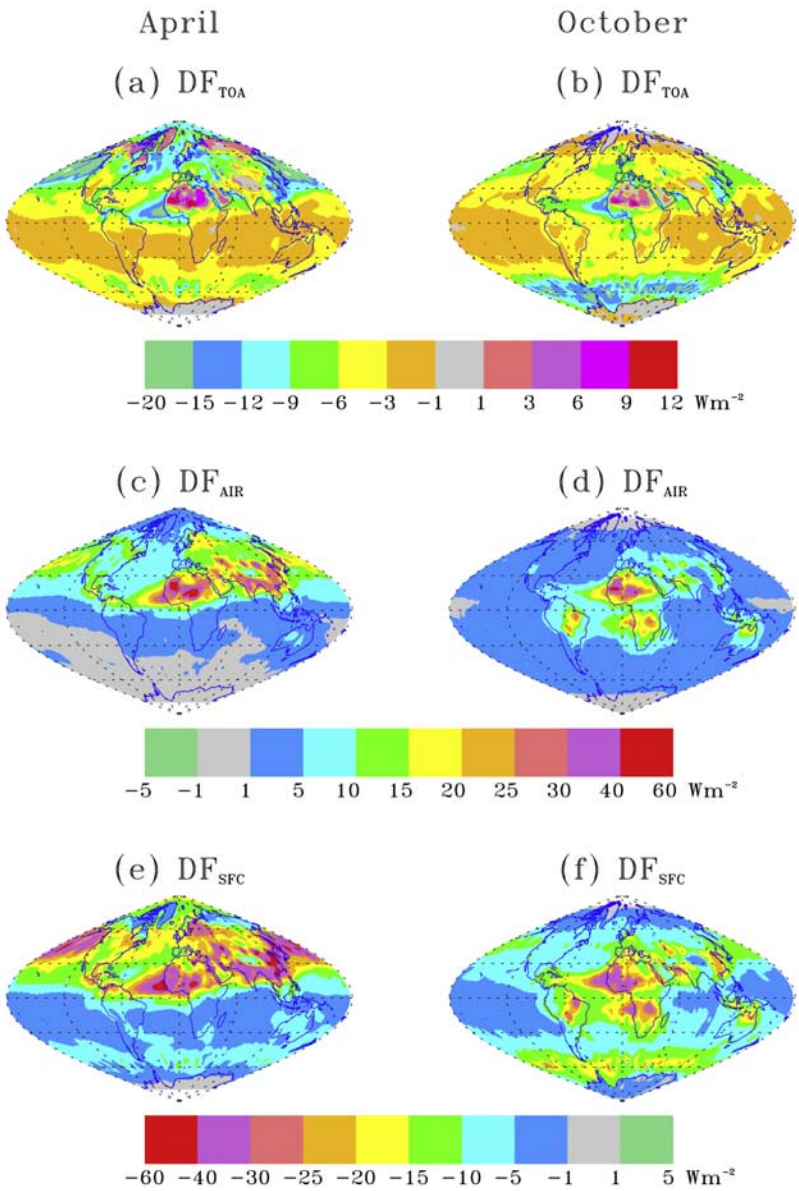

Figure 5. The direct solar perturbations (Wm^{-2}) at TOA (DF_{TOA}), atmosphere (DF_{AIR}) and surface (DF_{SFC}) by all aerosols for April (a, c, e) and October (b, d, f).